LETTER

doi:10.1038/nature09346

Conical intersection dynamics of the primary photoisomerization event in vision

Dario Polli[1], Piero Altoè[2], Oliver Weingart[3,4], Katelyn M. Spillane[5], Cristian Manzoni[1], Daniele Brida[1], Gaia Tomasello[2], Giorgio Orlandi[2], Philipp Kukura[6], Richard A. Mathies[5], Marco Garavelli[2] & Giulio Cerullo[1]

Ever since the conversion of the 11-*cis* retinal chromophore to its all-*trans* form in rhodopsin was identified as the primary photochemical event in vision[1], experimentalists and theoreticians have tried to unravel the molecular details of this process. The high quantum yield of 0.65 (ref. 2), the production of the primary ground-state rhodopsin photoproduct within a mere 200 fs (refs 3–7), and the storage of considerable energy in the first stable bathorhodopsin intermediate[8] all suggest an unusually fast and efficient photoactivated one-way reaction[9]. Rhodopsin's unique reactivity is generally attributed to a conical intersection between the potential energy surfaces of the ground and excited electronic states[10,11] enabling the efficient and ultrafast conversion of photon energy into chemical energy[12–16]. But obtaining direct experimental evidence for the involvement of a conical intersection is challenging: the energy gap between the electronic states of the reacting molecule changes significantly over an ultrashort timescale, which calls for observational methods that combine high temporal resolution with a broad spectral observation window. Here we show that ultrafast optical spectroscopy with sub-20-fs time resolution and spectral coverage from the visible to the near-infrared allows us to follow the dynamics leading to the conical intersection in rhodopsin isomerization. We track coherent wave-packet motion from the photoexcited Franck–Condon region to the photoproduct by monitoring the loss of reactant emission and the subsequent appearance of photoproduct absorption, and find excellent agreement between the experimental observations and molecular dynamics calculations that involve a true electronic state crossing. Taken together, these findings constitute the most compelling evidence to date for the existence and importance of conical intersections in visual photochemistry.

We initiated the photoisomerization reaction in the retinal chromophore of purified rhodopsin by 10-fs 500-nm pump pulses resonant with the ground-state absorption. The photoinduced dynamics were then probed by delayed ultra-broadband few-optical-cycle probe pulses, either in the visible wavelength region (500–720 nm) or in the near-infrared (NIR, 820–1,020 nm), generated by synchronized optical parametric amplifiers[17]. The temporal resolution was <20 fs over the entire monitored spectral range. Figure 1a presents a differential transmission ($\Delta T/T$) map as a function of probe wavelength and pump–probe time delay. Immediately following excitation from the ground state (S_0) to the first excited singlet state (S_1), we observed a positive $\Delta T/T$ signal (blue in the figure) with maximum intensity at ~650 nm, which is assigned to stimulated emission from the excited state due to the negligible ground-state absorption in this wavelength range. The stimulated emission signal rapidly shifts to the red while losing intensity and disappearing to wavelengths longer than 1,000 nm within ~75 fs. At this time, the $\Delta T/T$ signal changes sign and transforms into a weak photoinduced absorption signal (red in the figure), which initially appears at 1,000 nm and then gradually shifts to the blue and increases in intensity. For delays longer than 200 fs, the photoinduced absorption signal stabilizes as a long-lived band peaking at 560 nm, indicating the formation of the all-*trans* photoproduct[3]. We emphasize that the use of a sub-15-fs NIR probe is the key to observing the transition between the excited and ground electronic states. Time traces at selected probe wavelengths are shown in Fig. 1b, highlighting the red shift of the stimulated emission signal and the subsequent blue shift of the photoinduced absorption.

To extract a dynamic model of the photoinduced process from these data, we simulated the transient signals by using scaled complete active space–self consistent field (CASSCF) transition energies over hybrid quantum-mechanical (QM, CASSCF)/molecular-mechanical (MM) trajectories following the evolution of the opsin-embedded chromophore from the excited to the ground electronic state. Similar methods have been previously used to track photoinduced dynamics in rhodopsin[14,15,18] and other biomolecules[19–23]. This approach approximates

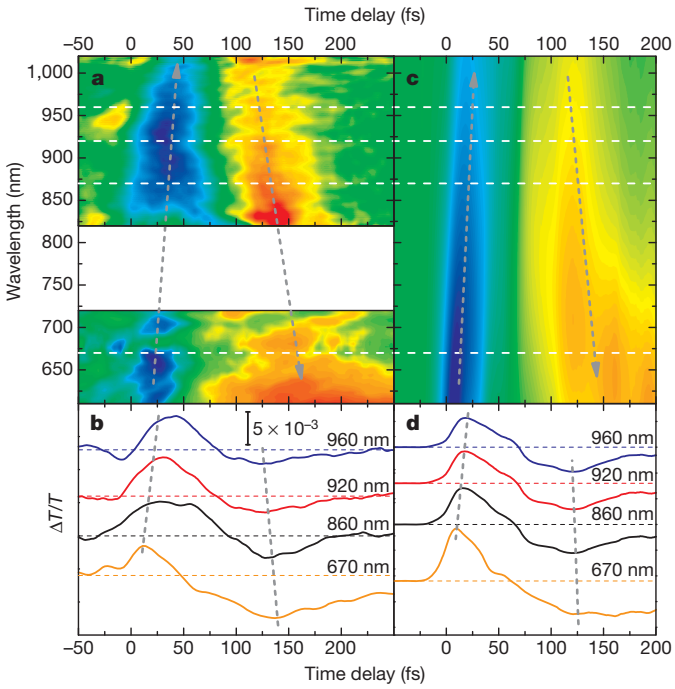

Figure 1 | Wave-packet dynamics through the rhodopsin conical intersection. a, **c**, Experimental (**a**) and simulated (**c**) differential transmission ($\Delta T/T$) map as a function of time delay and wavelength in the visible and NIR spectral regions. The white area in the experimental data around 750 nm corresponds to the 'blind region' of our set-up. Grey lines are guides to the eye, highlighting the temporal shifts of the stimulated emission (blue) and photoinduced absorption (red/orange) signals. **b**, **d**, Experimental (**b**) and simulated (**d**) $\Delta T/T$ dynamics at selected probe wavelengths.

[1]IFN-CNR, Dipartimento di Fisica, Politecnico di Milano, Piazza L. da Vinci 32, 20133 Milano, Italy. [2]Dipartimento di Chimica "G. Ciamician", Università di Bologna, V. F. Selmi 2, 40126 Bologna, Italy. [3]Lehrstuhl für theoretische Chemie, Universität Duisburg-Essen, Universitätsstrasse 5, 45117 Essen, Germany. [4]Max-Planck-Institut für Kohlenforschung, Kaiser-Wilhelm-Platz 1, 45470 Mülheim an der Ruhr, Germany. [5]Chemistry Department, University of California at Berkeley, Berkeley, California 94720, USA. [6]Department of Chemistry, University of Oxford, Physical and Theoretical Chemistry Laboratory, Oxford OX1 3QZ, UK.

full non-adiabatic complete active space with second-order perturbation theory (CASPT2) dynamics[24] that are currently possible only for smaller systems[25]. Our virtual spectroscopies and dynamics (Fig. 1c and d) agree almost quantitatively with the experimental results, owing to the inclusion of both the steric and electrostatic interactions within the retinal binding pocket (at the MM and QM level, respectively). The same holds for the 61% photoisomerization quantum yield and the average $S_1 \rightarrow S_0$ hopping time (~110 fs) extracted from the simulations, which further support the reliability of the theoretical approach.

The ultrafast complex spectral evolution observed both experimentally and theoretically can be understood qualitatively with the help of Fig. 2a. Here, the motion of the wave packet is depicted along the ground-state and excited-state potential energy surfaces of the rhodopsin chromophore as a function of the isomerization coordinate. The wave packet initially created in the Franck–Condon region of the excited state of the 11-*cis* reactant rapidly evolves along the reaction pathway towards the conical intersection, and the stimulated emission progressively shifts to the red as the energy gap between the excited and ground states narrows. Near the conical intersection region, which is reached in ~80 fs according to both experiment and theory, the stimulated emission signal vanishes as the two surfaces approach each other and the transition dipole moment decreases. Following the 'jump' to the hot ground state of the photoproduct, a symmetric photoinduced absorption signal is formed. This photoinduced absorption band rapidly shifts to the blue as the surfaces move away from each other energetically and the wave packet relaxes to the bottom of the photoproduct well, reflecting the redistribution of the excess energy deposited in the molecule and the final torsional movement to the all-*trans* configuration[26].

To complete the description of photoinduced dynamics in rhodopsin, we report the portion of the $\Delta T/T$ map probing the response of the system in the visible region, from 495 nm to 610 nm (Fig. 3a). In agreement with previous studies[3,27], we observe the delayed formation of the photoinduced absorption band of the photorhodopsin photoproduct, which peaks at 560 nm and is complete within 200–250 fs. The signal does not display exponential build-up dynamics, but appears rather abruptly, starting at ~150 fs (see time trace at 550 nm in Fig. 3b), which is the time needed for the wave packet to cross the conical intersection and enter the probed wavelength window on the photoproduct side. The blue region of the spectrum is dominated by the photobleaching signal from the ground state of the parent rhodopsin molecule, peaking at ~510 nm. These two spectral signatures partially overlap, so that the photobleaching band shrinks in time as the photoinduced absorption signal forms and blue-shifts. The amplitude of the photobleaching band also decreases owing to the

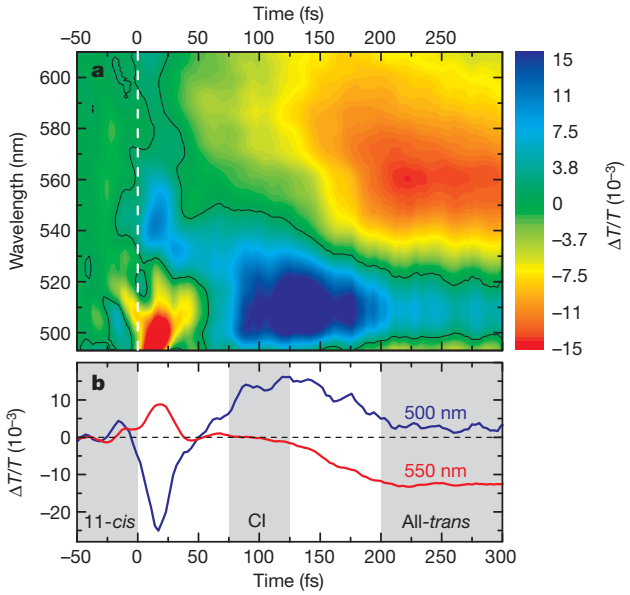

Figure 3 | Rhodopsin isomerization probed in the visible spectral range. **a**, $\Delta T/T$ map in the visible spectral region. **b**, Time traces at 500 nm and 550 nm probe wavelengths; central grey area labelled CI indicates the approximate conical intersection occurrence between the initial 11-*cis* configuration (left grey area) and the final all-*trans* (right grey area; reached in ~200 fs).

return of 35% of the excited state population back to the ground state of the 11-*cis* reactant. At early probe delays, a photoinduced absorption band peaking at ~500 nm is evident (see time trace in Fig. 3b), corresponding to a transition from the Franck–Condon excited state to a higher-lying S_n state[3], having a greater dipole moment than the ground state photobleaching band. This band disappears within ~50 fs, owing to the wave-packet motion out of the Franck–Condon region. Over longer timescales (see Supplementary Fig. 8 and Supplementary Discussion), the photoproduct photoinduced absorption signal displays vibrational coherence with a ~550-fs period (~60-cm^{-1} frequency). The probe-wavelength dependence of the amplitude and phase of this vibration is consistent with a wave packet moving in the ground state of the photoproduct, in agreement with previous observations[27].

The extremely high experimental time resolution combined with the remarkable agreement with theory makes it possible to confidently predict the real-time structural changes occurring within the first

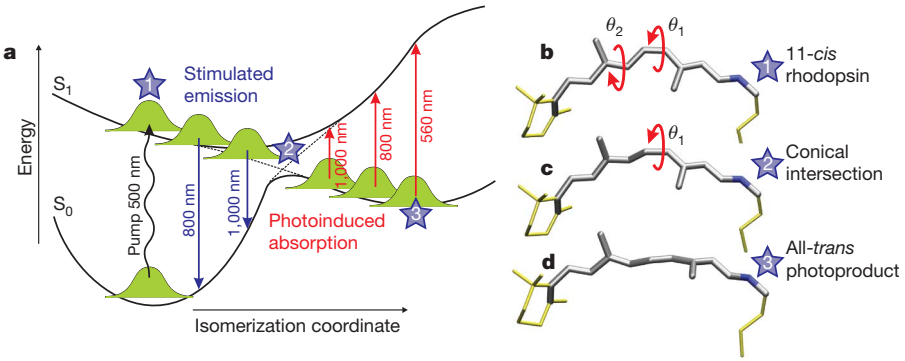

Figure 2 | Isomerization potential energy surfaces of rhodopsin. **a**, Sketch of the ground- and excited-state potential energy surfaces of the chromophore in rhodopsin as a function of the isomerization coordinate. Wavy arrow indicates photoexcitation, straight arrows correspond to stimulated emission (blue) or photoinduced absorption (red/orange). The graph shows that stimulated emission from the excited state of the parent molecule and photoinduced absorption from the hot photoproduct can monitor the wave-packet dynamics through the conical intersection. **b**–**d**, Averaged structures of the chromophore at the initial 11-*cis* (**b**) (blue star '1', $t = 0$ fs, $\theta_1 = -12.8°$, $\theta_2 = 173.9°$), conical intersection (**c**) (blue star '2', $t = 110$ fs, $\theta_1 = -87.8°$, $\theta_2 = -144.6°$) and final all-*trans* (**d**) (blue star '3', $t = 200$ fs, $\theta_1 = -141.0°$, $\theta_2 = -142.0°$) configurations; grey/yellow colours indicate the chromophore QM/MM regions in the simulations.

200 fs of retinal isomerization in rhodopsin. The Supplementary Movie shows the evolution of the reacting retinal structure during the first 200 fs, averaged over the isomerizing and non-isomerizing trajectories in the top and bottom movie panels, respectively. Here, we focus on the key structures, namely the 11-*cis* reactant, the structure of retinal at the conical intersection and the all-*trans* photoproduct (Fig. 2b–d). Comparison of the retinal structure in the ground state (Fig. 2b) with the structure at the conical intersection (Fig. 2c) reveals dramatic changes only in the vicinity of the isomerizing bond. We found that the average C11=C12 dihedral angle at the conical intersection is $\theta_1 = -87.8^\circ$ (Fig. 2c), ranging from -75° to -105° for individual trajectories, emphasizing the relevance of the C11=C12 twist in triggering internal conversion. At the same time, the C9=C10 torsional angle θ_2 also exhibits a large change (by $\sim 45^\circ$) on the excited-state surface as the wave packet moves towards the conical intersection (Fig. 2c). This torsion also persists on the photoproduct side (Fig. 2d), accounting for chromophore ends that are motionless during the isomerization process (yellow portions in Fig. 2b–d), in agreement with structures derived from femtosecond stimulated Raman scattering[26] and reminiscent of the 'bicycle pedal' proposal for retinal isomerization in rhodopsin[28,29]. Notably, all trajectories reach the S_1/S_0 crossing region and decay to S_0, from which they rapidly branch and immediately move towards their final ground state configuration: 61% yield the all-*trans* product ($\theta_1 \approx -140^\circ$), while 39% result in a frustrated isomerization and return to the *cis* reactant ($\theta_1 \approx -15^\circ$).

Taken together, these data indicate that the structural evolution from the reactant towards the conical intersection is restricted almost exclusively to the atoms in the centre of the molecule. This behaviour is promoted by the tight binding pocket provided by the protein for the chromophore, which restricts the possible motion at its ends[30]. Therefore, retinal can use all of the incident photon energy to drive minimal atomic displacements in the C9=C10–C11=C12 region and reach the conical intersection region within 80 fs, resulting in a very fast reaction speed. Once the local isomerization has taken place, the overall highly strained structure can then rapidly relax either in the photoproduct well, resulting in the more *trans*-like structure that completes the primary isomerization reaction (major component), or back to the 11-*cis* starting reactant (minor component). The close agreement between our experimental data and theoretical simulations indicates that the resulting molecular movie of the photoisomerization process, generated with atomistic detail and femtosecond time resolution, indeed reveals the complete dynamics of this classical conical intersection reaction that initiates vision.

METHODS SUMMARY

Ultrafast spectroscopy. An amplified Ti:sapphire laser system delivering 150-fs pulses at 790 nm and 1 kHz feeds three independent, synchronized non-collinear optical parametric amplifiers (NOPAs)[17]. The first generates 10-fs pulses centred at 520 nm (with 55-nm bandwidth) that are used to pump rhodopsin. The second and third NOPAs generate the probe pulses in the visible (500–750 nm, 7 fs) and in the NIR (820–1,020 nm, 13 fs). The sample is contained in a ~300-μm-pathlength cuvette and is flowed rapidly to ensure complete replacement between consecutive pulses. A fast spectrometer enables single-shot recording of the probe spectrum. Control runs on the buffer solution confirmed that the observed dynamics are solely due to rhodopsin molecules. Temporal resolution was limited by group-delay mismatch between pump and probe pulses in the cuvette to ~13 fs and ~18 fs at 700 nm and 900 nm, respectively.

Numerical simulations. Protein set-up (1U19 PDB code)[30] is documented elsewhere[16]. QM(CASSCF(10,10)/6-31G*)/MM(Amber99ff) calculations account for the chromophore/protein electrostatic (steric) interactions at the highest QM (MM) level. Figure 2 highlights the chromophore QM/MM regions that, together with the two neighbouring water molecules, are mobile. All other atoms are fixed at their crystallographic positions, a choice that is supported by the sub-200-fs reaction timescale and recent computational evidence[15]. A thermal sample (300 K) of 38 initial conditions is used. A velocity Verlet algorithm (step size ≤ 0.5 fs) is applied to propagate trajectories, at constant energy, by equally weighting the first three roots in a state average CAS(10/10) procedure. $S_1 \rightarrow S_0$ decay occurs according to the scalar product of the S_1 and S_0 state coefficients ($\Delta E_{S0/S1} < 2.2$ kcal mol^{-1} at hopping). CASSCF data for $S_1 \rightarrow S_0$, $S_1 \rightarrow S_2$ and $S_0 \rightarrow S_1$ transitions from individual trajectories are convolved with a 20-fs FWHM (full-width at half-maximum) Gaussian function and scaled to match CASPT2-corrected energy gaps.

Full Methods and any associated references are available in the online version of the paper at www.nature.com/nature.

Received 13 May 2009; accepted 2 July 2010.

1. Yoshizawa, T. & Wald, G. Pre-lumirhodopsin and the bleaching of visual pigments. *Nature* **197,** 1279–1286 (1963).
2. Kim, J. E., Tauber, M. J. & Mathies, R. A. Wavelength dependent *cis-trans* isomerization in vision. *Biochemistry* **40,** 13774–13778 (2001).
3. Schoenlein, R. W., Peteanu, L. A., Mathies, R. A. & Shank, C. V. The first step in vision: femtosecond isomerization of rhodopsin. *Science* **254,** 412–415 (1991).
4. Haran, G., Morlino, E. A., Matthes, J., Callender, R. H. & Hochstrasser, R. M. Femtosecond polarized pump-probe and stimulated emission spectroscopy of the isomerization reaction of rhodopsin. *J. Phys. Chem. A* **103,** 2202–2207 (1999).
5. Chosrowjan, H. *et al.* Rhodopsin emission in real time: a new aspect of the primary event in vision. *J. Am. Chem. Soc.* **120,** 9706–9707 (1998).
6. Kandori, H. *et al.* Excited-state dynamics of rhodopsin probed by femtosecond fluorescence spectroscopy. *Chem. Phys. Lett.* **334,** 271–276 (2001).
7. Kochendoerfer, G. G. & Mathies, R. A. Spontaneous emission study of the femtosecond isomerization dynamics of rhodopsin. *J. Phys. Chem.* **100,** 14526–14532 (1996).
8. Schick, G. A., Cooper, T. M., Holloway, R. A., Murray, L. P. & Birge, R. R. Energy storage in the primary photochemical events of rhodopsin and isorhodopsin. *Biochemistry* **26,** 2556–2562 (1987).
9. Mathies, R. A. & Lugtenburg, J. in *Handbook of Biological Physics* Vol. 3, *Molecular Mechanisms in Visual Transduction* (eds Stavenga, D. G., DeGrip, W. J. & Pugh E. N.) 55–90 (Elsevier Science, 2000).
10. Garavelli, M., Celani, P., Bernardi, F., Robb, M. A. & Olivucci, M. The $C_5H_6NH_2^+$ protonated Shiff base: an *ab initio* minimal model for retinal photoisomerization. *J. Am. Chem. Soc.* **119,** 6891–6901 (1997).
11. González-Luque, R. *et al.* Computational evidence in favor of a two-state, two-mode model of the retinal chromophore photoisomerization. *Proc. Natl Acad. Sci. USA* **97,** 9379–9384 (2000).
12. Klessinger, M. & Michl, J. *Excited States and Photochemistry of Organic Molecules* (VCH, 1994).
13. Levine, B. G. & Martinez, T. M. Isomerization through conical intersections. *Annu. Rev. Phys. Chem.* **58,** 613–634 (2007).
14. Frutos, L. M., Andruniow, T., Santoro, F., Ferre, N. & Olivucci, M. Tracking the excited-state time evolution of the visual pigment with multiconfigurational quantum chemistry. *Proc. Natl Acad. Sci. USA* **104,** 7764–7769 (2007).
15. Hayashi, S., Tajkhorshid, E. & Schulten, K. Photochemical reaction dynamics of the primary event of vision studied by means of a hybrid molecular simulation. *Biophys. J.* **96,** 403–416 (2009).
16. Tomasello, G. *et al.* Electrostatic control of the photoisomerization efficiency and optical properties in visual pigments: on the role of counterion quenching. *J. Am. Chem. Soc.* **131,** 5172–5186 (2009).
17. Manzoni, C., Polli, D. & Cerullo, G. Two-color pump-probe system broadly tunable over the visible and the near infrared with sub-30 fs temporal resolution. *Rev. Sci. Instrum.* **77,** 023103 (2006).
18. Weingart, O. The twisted C11=C12 bond of the rhodopsin chromophore — a photochemical hot spot. *J. Am. Chem. Soc.* **129,** 10618–10619 (2007).
19. Hayashi, S., Tajkhorshid, E. & Schulten, K. Molecular dynamics simulation of bacteriorhodopsin's photoisomerization using *ab initio* forces for the excited chromophore. *Biophys. J.* **85,** 1440–1449 (2003).
20. Groenhof, G. *et al.* Photoactivation of the photoactive yellow protein: why photon absorption triggers a *trans*-to-*cis* isomerization of the chromophore in the protein. *J. Am. Chem. Soc.* **126,** 4228–4233 (2004).
21. Groenhof, G. *et al.* Ultrafast deactivation of an excited cytosine-guanine base pair in DNA. *J. Am. Chem. Soc.* **129,** 6812–6819 (2007).
22. Hudock, H. R. *et al. Ab initio* molecular dynamics and time-resolved photoelectron spectroscopy of electronically excited uracil and thymine. *J. Phys. Chem. A* **111,** 8500–8508 (2007).
23. Hudock, H. R. & Martinez, T. J. Excited-state dynamics of cytosine reveal multiple intrinsic subpicosecond pathways. *ChemPhysChem* **9,** 2486–2490 (2008).
24. Andersson, K., Malmqvist, P.-A. & Roos, B. O. Second-order perturbation theory with a complete active space self-consistent field reference function. *J. Chem. Phys.* **96,** 1218–1226 (1992).
25. Tao, H., Levine, B. G. & Martinez, T. J. *Ab initio* multiple spawning dynamics using multi-state second-order perturbation. *J. Phys. Chem. A* **113,** 13656–13662 (2009).
26. Kukura, P., McCamant, D. W., Yoon, S., Wandschneider, D. B. & Mathies, R. A. Structural observation of the primary isomerization in vision with femtosecond-stimulated Raman. *Science* **310,** 1006–1009 (2005).
27. Wang, Q., Schoenlein, R. W., Peteanu, L. A., Mathies, R. A. & Shank, C. V. Vibrationally coherent photochemistry in the femtosecond primary event of vision. *Science* **266,** 422–424 (1994).
28. Warshel, A. Bicycle-pedal model for the first step in the vision process. *Nature* **260,** 679–683 (1976).

29. Warshel, A. & Barboy, N. Energy storage and reaction pathways in the first step of the vision process. *J. Am. Chem. Soc.* **104,** 1469–1476 (1982).
30. Okada, T. *et al.* The retinal conformation and its environment in rhodopsin in light of a new 2.2 Å crystal structure. *J. Mol. Biol.* **342,** 571–583 (2004).

Supplementary Information is linked to the online version of the paper at www.nature.com/nature.

Acknowledgements M.G., O.W., G.O., G.T. and P.A. thank E4-Computer Engineering S.p.A. for computational time and technical assistance. Part of this study was financially supported by the DFG (FOR490) and by the PRIN programme (2008JKBBK4). P.K. is supported by a Career Acceleration Fellowship awarded by the UK Engineering and Physical Sciences Research Council (EP/H003541/1).

Author Contributions R.A.M., P.K., M.G. and G.C. conceived the project and contributed the original scientific ideas to this work. D.P., C.M. and D.B. executed the experiments. K.M.S. carried out rhodopsin sample preparation/purification. P.A., O.W. and G.O. planned calculations, P.A. and O.W. executed them. G.T. collected calibration data. All authors discussed the results and contributed to the preparation of the manuscript.

Author Information Reprints and permissions information is available at www.nature.com/reprints. The authors declare no competing financial interests. Readers are welcome to comment on the online version of this article at www.nature.com/nature. Correspondence and requests for materials should be addressed to M.G. (marco.garavelli@unibo.it; theory) and G.C. (giulio.cerullo@fisi.polimi.it; experiments).

METHODS

Sample preparation. Rhodopsin molecules were extracted from the rod outer segments of bovine retinae and purified by sucrose flotation followed by sucrose density gradient centrifugation, as described elsewhere[31]. The OD_{280}/OD_{500} absorbance ratio was less than 1.8. Fresh NH_2OH was added to a final concentration of 2 mM.

Pump-probe spectroscopy. Supplementary Fig. 1 shows the schematic experimental set-up. It starts with a regeneratively amplified mode-locked Ti:sapphire laser system (Clark-MXR model CPA-1) delivering pulses with 150-fs duration, 500-μJ energy, at 1-kHz repetition rate and 780-nm central wavelength. The system drives three independent non-collinear optical parametric amplifiers (NOPAs)[17] in the visible and in the NIR, which generate the pump and the probe pulses for the time-resolved experiments. The first NOPA (NOPA1) generates the pump pulses in the 500- to 550-nm wavelength region in order to selectively excite the rhodopsin molecule in resonance with its ground-state absorption. The second and third NOPAs are used alternatively to generate the probe pulses in the visible (NOPA2, from 500 nm to 750 nm) or in the NIR frequency range (NOPA3, from 820 nm to 1,020 nm). NOPA1 and NOPA2 are compressed to their transform-limited (TL) duration by multiple bounces on custom-designed chirped mirrors, while NOPA3 is compressed to the TL by a Brewster-cut fused-silica prism pair. The pulse durations, retrieved using the frequency-resolved optical gating (FROG) technique, are 10 fs for NOPA1, 7 fs for NOPA2 and 13 fs for NOPA3. Supplementary Fig. 2 shows typical spectra from the three NOPAs.

The sample is contained in a cuvette with 250-μm-thick fused-silica windows and ~300-μm optical path. The sample thickness ultimately determines our experimental temporal resolution due to group-delay mismatch between the pump pulse (in the blue) and the probe pulse (in the red/NIR): when the pump and probe pulses are perfectly synchronized (time zero) at the front face of the sample, they will be delayed at the sample exit, thus smearing out the measured time traces. The calculated group delay mismatch is 12.7 fs at 700 nm and 17.4 fs at 900 nm (considering the dispersion relations of water).

After the sample, the probe beam is selected by an iris and focused onto the entrance slit of a spectrometer equipped with a 1,024-pixel linear photodiode array and electronics specially designed for fast read-out times and low noise[32]. The spectral resolution of the spectrograph (about 2 nm) is more than sufficient for our experiments. A fast analogue-to-digital conversion card with 16-bit resolution enables single-shot recording of the probe spectrum at the full 1-kHz repetition rate. By recording pump-on and pump-off probe spectra, we can calculate the $\Delta T/T$ spectrum at the specific probe delay τ as:

$$\Delta T/T(\lambda,\tau) = [T_{on}(\lambda,\tau) - T_{off}(\lambda)]/T_{off}(\lambda)$$

By repeating this procedure for a few hundred milliseconds and averaging the resulting signals, it is thus possible to achieve a high enough signal-to-noise ratio to detect $\Delta T/T$ spectra down to the 10^{-4} level over the whole probe wavelength range. By moving the translation stage we record $\Delta T/T$ spectra at different probe delays, thus obtaining a complete two-dimensional map: $\Delta T/T = \Delta T/T(\lambda,\tau)$.

The absorption spectrum of rhodopsin, peaking at ~500 nm, is plotted in Supplementary Fig. 2 as a shaded curve. To prevent the accumulation of photoproduct in the irradiated volume, the sample was continuously re-circulated by means of a peristaltic pump in a closed-loop circuit with ~4 ml total volume to ensure complete replacement of the sample in the focal volume for each consecutive laser shot. The excitation fluence was chosen so as to be in a perturbative regime, with maximum $|\Delta T/T|$ of the order of 1–2%.

To ensure that the signal is only due to the rhodopsin molecule, we also performed pump-probe experiments, in exactly the same experimental conditions, on two different samples: (1) the buffer alone and (2) the fully bleached rhodopsin solution obtained by stopping the flow. In both cases, the transient signal disappeared except for the coherent artefact around time zero, which was subtracted from the data.

QM/MM calculations and protein setup. CASPT2//CASSCF/6-31G*/AMBER QM/MM (ref. 33) computations are performed using the COBRAMM interface[34] implemented by our group, using a hydrogen link-atom scheme[35] and linking the Molpro[36], MOLCAS-6.0[37] and AMBER8[38] packages. Details of the approach have been presented elsewhere[34]. Other applications involving this methodology may be found in refs 16, 39. Geometry optimizations, frequency calculations and molecular dynamics involve *ab initio* CASSCF/6-31G* computations[40] for the QM region. The AMBER8 software and the *ff99* force field[38] are used for the MM region and its charges. During all calculations the retinal chromophore, the region between Schiff base nitrogen and the C_β-carbon of Lys 296, and the two neighbouring water molecules are mobile. The remaining atoms are fixed at their positions in the protein crystal (1U19 PDB code). Two different chromophore QM/MM-models have been used here, a full chromophore set-up for optimizations and static isomerization path mapping, and a reduced chromophore model for molecular dynamics simulations. In the full chromophore the QM-MM frontier is placed at the C_δ–C_ε bond of the Lys 296 side chain and a full CASSCF active space of 12 electrons and 12 π orbitals (CAS 12/12) is applied. The reduced model is simplified by excluding the non-π-conjugated β-ionone ring part (see Fig. 2b–d) and employing a reduced CASSCF 10/10 active space.

The protein set-up used in this work is the same used by some of the authors in a very recent static investigation of rhodopsin photoisomerization (see ref. 16 for the details). While the protonation state of glutamic acid 181 is still a matter of debate, it was left unprotonated in the current simulations. Owing to its location above the centre of the retinal chromophore, this residue's charge does not affect the photoisomerization path and the energy of the photoactive charge transfer state S_1 (refs 16, 41). Therefore, this choice should not influence the computed dynamics.

Active space selection for dynamical simulations. The π orbital set used for the reduced chromophore is depicted in Supplementary Fig. 3. To validate the reductions in orbital space and QM region, the static excited state reaction path along C11 = C12 torsion was computed by constrained geometry optimization and compared to the corresponding reaction path of the full chromophore from ref. 16. A two root state averaged wavefunction was employed in both calculations. Supplementary Fig. 4 shows the isomerization S_1 energy profiles for the full chromophore (full lines) and the reduced model (dotted lines). Both the excited state energies and the S_1/S_0 energy differences in CAS(12/12) are almost perfectly reproduced by CAS(10/10). From these results we conclude that the simplifications applied are reasonable and allow a calculation of several trajectories at significantly reduced computational cost, still preserving the accuracy found in the unreduced QM-model/active space. This conclusion is further supported by dynamical computations (see below).

Molecular dynamics simulations. CAS(10,10)/6-31G*/AMBER QM/MM numerical frequencies have been calculated on the rhodopsin ground state minimum (optimized at the same level). These are used to generate initial conditions for the dynamics by thermally sampling the vibrational modes at 300 K (ref. 42; including zero-point energy corrections: high frequency C–H, N–H and O–H modes are excluded). Note that the temperature distribution is related only to the mobile part, while the protein stays fixed during thermal sampling and molecular dynamics runs. The fixed crystal structure of the protein is considered as a mean representation of the experimental positions of the atoms, although at low (100 K) temperature. This approximation is justified by the extremely short timescale of the rhodopsin primary photochemical event investigated here (~100 fs decay time and 200 fs photoproduct appearance time) that prevents protein thermalization (that is, equilibration). This is further supported by the results of ref. 15, showing that excited state dynamics in rhodopsin are not affected by protein mobility. While this is a well established procedure[14,16], it was also adopted for practical reasons. The number of electrostatic field derivatives that can be calculated in one step by the *ab initio* program is limited. Furthermore, a mobile protein environment may result in a wrong ordering of S_1 and S_2 energy states at the CASSCF level, leading to unrealistic simulations. Supplementary Fig. 5 shows the distribution of several ensemble parameters for the 38 randomly generated initial conditions. Considering the limited number of sampled points, the partitioning of potential and kinetic energies and torsion angles appears reasonable and suggests that the sample is already statistically meaningful.

Trajectories were started after Franck–Condon excitation to the first excited singlet state using the COBRAMM interface, which couples Molpro-CASSCF and Amber. The wavefunction was averaged over the first three singlet states throughout the entire calculation. For accurate calculation of state averaged CASSCF gradients, Molpro's CPMCSCF routines were employed[36]. Newton's equations of motion were integrated on the fly using the velocity Verlet algorithm[43] and a time step of 0.5 fs. In order to properly detect possible decay points, the time step was reduced to 0.25 fs when the S_1–S_0 energy difference was below 8 kcal mol^{-1}. When the scalar product of the S_1 and S_0 state coefficients indicated that a surface crossing had been passed, the trajectories were brought to the ground state[44]. The energy gap at the hops was always below 2.2 kcal mol^{-1}. This simplified algorithm forces hops to take place only at the S_1/S_0 intersection seam and, in principle, could lead to an underestimation of the population transfer probability. However, the S_1/S_0 conical intersection is very peaked in rhodopsin[16]. This topological feature is compatible with a decay that substantially occurs only when the intersection seam is reached, justifying the adopted hopping procedure.

The two-panel Supplementary Movie displays the 'averaged' molecular structures corresponding to the trajectories leading respectively to the all-*trans* retinal photoproduct and to the 11-*cis* reactant; owing to the random rotation of methyls, the positions of methyl hydrogens have been fixed relative to their neighbouring carbon. The dihedral angle of the rotating central bond is explicitly displayed, clearly showing that the motion is restricted to the central part of the chromophore.

Reference trajectories: further validation of the reduced CAS(10,10) active space. Two reference trajectories, starting without initial kinetic energy (0 K) with a time step of 1 fs, were propagated employing the reduced QM chromophore model with a CAS(10/10) active space and a full CAS(12/12) active space description. Supplementary Fig. 6 shows the evolution of energies, C11 = C12 dihedrals and bond lengths. For the most part, the two trajectories are almost identical. Subtle differences appear only after the hop to the ground state, which is delayed by only 1 fs in CAS(12/12). These dynamical results validate the reduced CAS(10/10) active space employed in this work for a systematic dynamical investigation of the retinal photoreaction in rhodopsin, being almost as accurate as the full CAS(12,12) active space.

Calibration of ultraviolet–visible absorption and emission data. In order to partially account for the deficiencies in CASSCF calculated spectral data, linear scaling factors were estimated to match the more accurate values obtained at the CASPT2 level of theory[24]. As applied in the dynamics, a CAS(10,10)/6-31G* three root state averaged description of the wavefunction was used for the reduced system to optimize the complete static photoisomerization path from first excited to ground state. State averaged CASSCF gradients were computed using Molpro's CPMCSCF routines. The three root state averaged approach allowed us to estimate the contribution of both S_0–S_1 and S_1–S_2 transitions; the latter may have a non-negligible influence on time-resolved emission/absorption spectra.

Supplementary Fig. 7a shows the first three singlet state energies along the aforementioned reaction path calculated with CASSCF (full lines) and with Molcas CASPT2 (dotted lines). To generate these plots, the CASSCF(10/10) optimized reaction path of the reduced model (full lines) has been re-evaluated at the CASPT2 level employing a constant imaginary level shift[45] of 0.2 and according to a full chromophore approach: the QM region and active space have been enlarged on top of the reduced chromophore structures to embrace the whole chromophore and π orbital space, respectively. Remarkably, the vertical $S_0 \rightarrow S_1$ CASPT2(12,12) computed energy is 58.9 kcal mol^{-1}, in fair agreement with the recorded absorption (57.6 kcal mol^{-1}). As expected, S_1 is less steep at the CASPT2 level, and the S_2 energy is significantly reduced when considering dynamic electron correlation. Energy differences are depicted in Supplementary Fig. 7b. Scaling factors for the stimulated emission signal were obtained by averaging the energy difference quotients from the S_1 backbone relaxed chromophore structure (Min-S_1) to 60° of C10–C11=C12–C13 torsion. It is worth noting that, in order to increase the accuracy of the scaling factors employed in spectra simulations, both the Franck–Condon structure and the region in close vicinity to the conical intersection (that is, 70°–110° twisted points that all have a rather small S_1/S_0 energy gap) have not been taken into account in the fitting, as they do not enter the probe wavelength window (610–720 nm and 820–1,020 nm) of the experiments (see Fig. 1). Scaling factors for the photoinduced absorption signal were estimated by an analogous procedure, using the optimized ground state path from 120° towards the photoproduct. The values are reported in Supplementary Table 1.

In addition, the scaling factor for the stimulated emission process has also been determined from the reference 0 K CAS(10/10) trajectory described in the previous section, by employing an analogous procedure. Those values are listed in Supplementary Table 2 and show that the dynamical scaling factor (0.793) is very similar to the static one (0.791). This confirms that the scaling factors obtained here are applicable to retinal photoisomerization trajectories.

Supplementary Fig. 7, comparing CASSCF versus CASPT2 energy profiles, also illustrates another important point: the CASSCF surface is not much steeper than the correlated one. Indeed, CASSCF overestimates excited state energies all along the photoisomerization path including the starting (Franck–Condon) and ending (conical intersection) points, leading to a moderate change in the gradient. More specifically, both profiles are barrierless and only the very initial part (Franck–Condon→Min-S_1) of the CASSCF relaxation path is slightly steeper. This part refers mainly to C–C bond order inversion, with no torsion involved. Afterwards, when C11 = C12 rotation becomes active, the two surfaces run almost parallel to each other. The same behaviour has already been recognized in other retinal protonated Schiff base models (see figure 3 in ref. 10).

Owing to the overestimation of the surface steepness, a somewhat faster process is expected in our simulations and, indeed, our initial relaxation out of the Franck–Condon region is slightly faster than observed: see the simulated lines in Fig. 1c that are steeper than the experimental ones in Fig. 1a. However, the C11 = C12 torsional mode is driven by a correct gradient and force field, and the timing error is comparable to the 20-fs time resolution of the experiments. For this reason, differently from ref. 14, we preferred not to apply any scaling factor to the simulated timescale, which already agrees reasonably well with the experiments. The scaling factor was instead applied to the transition energies to gain experimentally accurate values.

From the trajectories to the transient spectra. For each instant of time, the transient spectrum was calculated as a superposition of $S_1 \rightarrow S_0$ stimulated emission and $S_1 \rightarrow S_2$ photoinduced absorption before, and $S_0 \rightarrow S_1$ photoinduced absorption after, the hop to the ground state. Each of these three signals was represented by a Gaussian functions centred at the corresponding transition energy averaged over all the trajectories with half-width equal to the standard deviation of the collected data and height equal to the mean oscillator strength. To account for the finite pulsewidths used in the experiments, we convolved the calculated transient signals with a 20-fs FWHM Gaussian function.

31. De Grip, W. J., Daemen, F. J. M. & Bonting, S. L. Isolation and purification of bovine rhodopsin. *Methods Enzymol.* **67,** 301–320 (1980).
32. Polli, D., Lüer, L. & Cerullo, G. High-time-resolution pump-probe system with broadband detection for the study of time-domain vibrational dynamics. *Rev. Sci. Instrum.* **78,** 103108 (2007).
33. Lin, H. & Truhlar, D. G. QM/MM: what have we learned, where are we, and where do we go from here? *Theor. Chem. Acc.* **117,** 185–199 (2007).
34. Altoè, P., Stenta, M., Bottoni, A. & Garavelli, M. A tunable QM/MM approach to chemical reactivity, structure and physico-chemical properties prediction. *Theor. Chem. Acc.* **118,** 219–240 (2007).
35. Singh, U. C. & Kollman, P. A. A combined *ab initio* quantum mechanical and molecular mechanical method for carrying out simulations on complex molecular systems: applications to the $CH_3Cl + Cl^-$ exchange reaction and gas phase protonation of polyethers. *J. Comput. Chem.* **7,** 718–730 (1986).
36. Werner, H.-J. *et al.* MOLPRO, version 2008.1, a package of *ab initio* programs. (Cardiff University, UK, 2008).
37. Karlström, G. *et al.* MOLCAS: a program package for computational chemistry. *Comput. Mater. Sci.* **28,** 222–239 (2003).
38. Case, D. A. *et al.* The Amber biomolecular simulation programs. *J. Comput. Chem.* **26,** 1668–1688 (2005).
39. Stenta, M. *et al.* The catalytic activity of proline racemase: a quantum mechanical/molecular mechanical study. *J. Phys. Chem. B* **112,** 1057–1059 (2008).
40. Roos, B. O. in *Advances in Chemical Physics: Ab Initio Methods in Quantum Chemistry* Part 2, Vol. 69 (ed. Lawley, K. P.) 399–446 (Wiley & Sons, 1987).
41. Cembran, A., Bernardi, F., Olivucci, M. & Garavelli, M. Counterion controlled photoisomerization of retinal chromophore models: a computational investigation. *J. Am. Chem. Soc.* **126,** 16018–16037 (2004).
42. Sloane, C. S. & Hase, W. L. On the dynamics of state selected unimolecular reactions: chloroacetylene dissociation and predissociation. *J. Chem. Phys.* **66,** 1523–1533 (1977).
43. Verlet, L. Computer ''experiments'' on classical fluids. I. Thermodynamical properties of Lennard-Jones molecules. *Phys. Rev.* **159,** 98–103 (1967).
44. Weingart, O., Schapiro, I. & Buss, V. Photochemistry of visual pigment chromophore models by *ab initio* molecular dynamics. *J. Phys. Chem. B* **111,** 3782–3788 (2007).
45. Forsberg, N. & Malmqvist, P.-Å. Multiconfiguration perturbation theory with imaginary level shift. *Chem. Phys. Lett.* **274,** 196–204 (1997).